



## Critical thickness for the emergence of Weyl features in $\text{Co}_3\text{Sn}_2\text{S}_2$ thin films

Junya Ikeda<sup>1</sup>, Kohei Fujiwara <sup>1✉</sup>, Junichi Shiogai<sup>1</sup>, Takeshi Seki<sup>1,2</sup>, Kentaro Nomura<sup>1,2</sup>, Koki Takanashi<sup>1,2,3</sup> & Atsushi Tsukazaki <sup>1,2✉</sup>

Magnetic Weyl semimetals are quantum phases of matter arising from the interplay of linearly dispersive bands, spin-orbit coupling, and time reversal symmetry breaking. This can be realised, for example, in  $\text{Co}_3\text{Sn}_2\text{S}_2$ , based on a cobalt kagome lattice and characterised by intriguing phenomena such as large anomalous Hall effect, Nernst effect, and water oxidation. Here, we attempt to determine the robustness of the twofold necessary conditions for the emergence of the magnetic Weyl semimetal phase in  $\text{Co}_3\text{Sn}_2\text{S}_2$  ultrathin films. Except for two-dimensional layered materials, a reduction of thickness generally makes it difficult to develop topological character and ferromagnetic long-range order. In  $\text{Co}_3\text{Sn}_2\text{S}_2$  films, while ferromagnetic ordering appears robustly even in average thicknesses of one or two unit cells with island-like polycrystalline domains, the anomalous Hall conductivity appears only above a critical thickness of approximately 10 nm. The emergence of surface conduction and large anomalous Hall effect implies the distinct contribution of Weyl nodes and their Berry curvature. These findings reveal an exotic feature of Weyl physics in thin-film based superstructures as well as a potential for future applications in electronic devices.

<sup>1</sup>Institute for Materials Research, Tohoku University, Sendai, Japan. <sup>2</sup>Center for Spintronics Research Network (CSRN), Tohoku University, Sendai, Japan. <sup>3</sup>Center for Science and Innovation in Spintronics (CSIS), Core Research Cluster, Tohoku University, Sendai, Japan. ✉email: [kfujiwara@imr.tohoku.ac.jp](mailto:kfujiwara@imr.tohoku.ac.jp); [tsukazaki@imr.tohoku.ac.jp](mailto:tsukazaki@imr.tohoku.ac.jp)

Of proposed magnetic Weyl semimetals (mWSMs)<sup>1–4</sup>, particular interest has been focused on  $\text{Co}_3\text{Sn}_2\text{S}_2$  with a kagome lattice of Co<sup>5–10</sup>, three layers of which are stacked in one unit cell of the crystal structure (Fig. 1a). The electronic structure of  $\text{Co}_3\text{Sn}_2\text{S}_2$  is schematically drawn in Fig. 1b. Finite contribution of spin-orbit coupling (SOC) produces a gap at the band crossing points except for the protected spatial symmetry positions (from left to centre of Fig. 1b). This is defined as Dirac semimetal (DSM) with possessing helical Fermi arcs (FAs). With broken time-reversal symmetry, the mWSM phase emerges with chiral FAs owing to ferromagnetic exchange splitting (right of Fig. 1b). On the projected surface normal to the plane of  $\text{Co}_3\text{Sn}_2\text{S}_2$  films (Fig. 1c), the surface FAs contribute to provide electrical conduction because the pairs of Weyl nodes are tilted from the magnetisation direction along  $z$  axis<sup>9</sup>. The Weyl nodes in the electronic bands enlarge the summation of Berry curvature under the well-regulated Fermi energy ( $E_F$ )<sup>10</sup>, inducing the large anomalous phenomena<sup>5–7</sup>. Ultimately, the emergence of the quantum anomalous Hall effect has been theoretically proposed in the monolayer of the kagome lattice<sup>11</sup> in  $\text{Co}_3\text{Sn}_2\text{S}_2$ <sup>12</sup>.

While the benefit of the SOC is maintained in the ultrathin films, the robustness of the mWSM phase against the thickness reduction is independently influenced by the twofold stability of

linear dispersive band and ferromagnetism. On the one hand, for topological materials such as three-dimensional topological insulators and DSMs, the topological phase disappears in ultrathin films owing to topological phase transition driven by hybridisation of surface states<sup>13,14</sup> and crossover by quantum size effect<sup>15</sup>, respectively. On the other hand, the stability of ferromagnetism in the thin-limit is an unresolved fundamental problem in  $\text{Co}_3\text{Sn}_2\text{S}_2$ . The itinerant ferromagnetism in the kagome lattice of  $\text{Co}_3\text{Sn}_2\text{S}_2$  is generally considered with the Stoner mechanism<sup>16,17</sup>. Except for two-dimensional layered compounds such as  $\text{CrI}_3$ <sup>18</sup> and  $\text{Cr}_2\text{Ge}_2\text{Te}_6$ <sup>19</sup>, however, it has been well known that the ferromagnetic order becomes drastically weakened in the thin-limit of conventional ferromagnetic metals<sup>20,21</sup>.

Because of the difficulty in the exfoliation from bulk  $\text{Co}_3\text{Sn}_2\text{S}_2$  crystals, we investigate the magnetisation and electrical transport properties in the films approaching the thin-limit by careful synthesis of  $\text{Co}_3\text{Sn}_2\text{S}_2$  thin films with the varied film thickness  $t$  using vacuum deposition technique. We here disclose the robustness of mWSM phase in  $\text{Co}_3\text{Sn}_2\text{S}_2$  via characterisation of ferromagnetism and Weyl transport features in  $\text{Co}_3\text{Sn}_2\text{S}_2$  thin films. While the ferromagnetism with perpendicular magnetic anisotropy persists down to a few unit cell thicknesses with

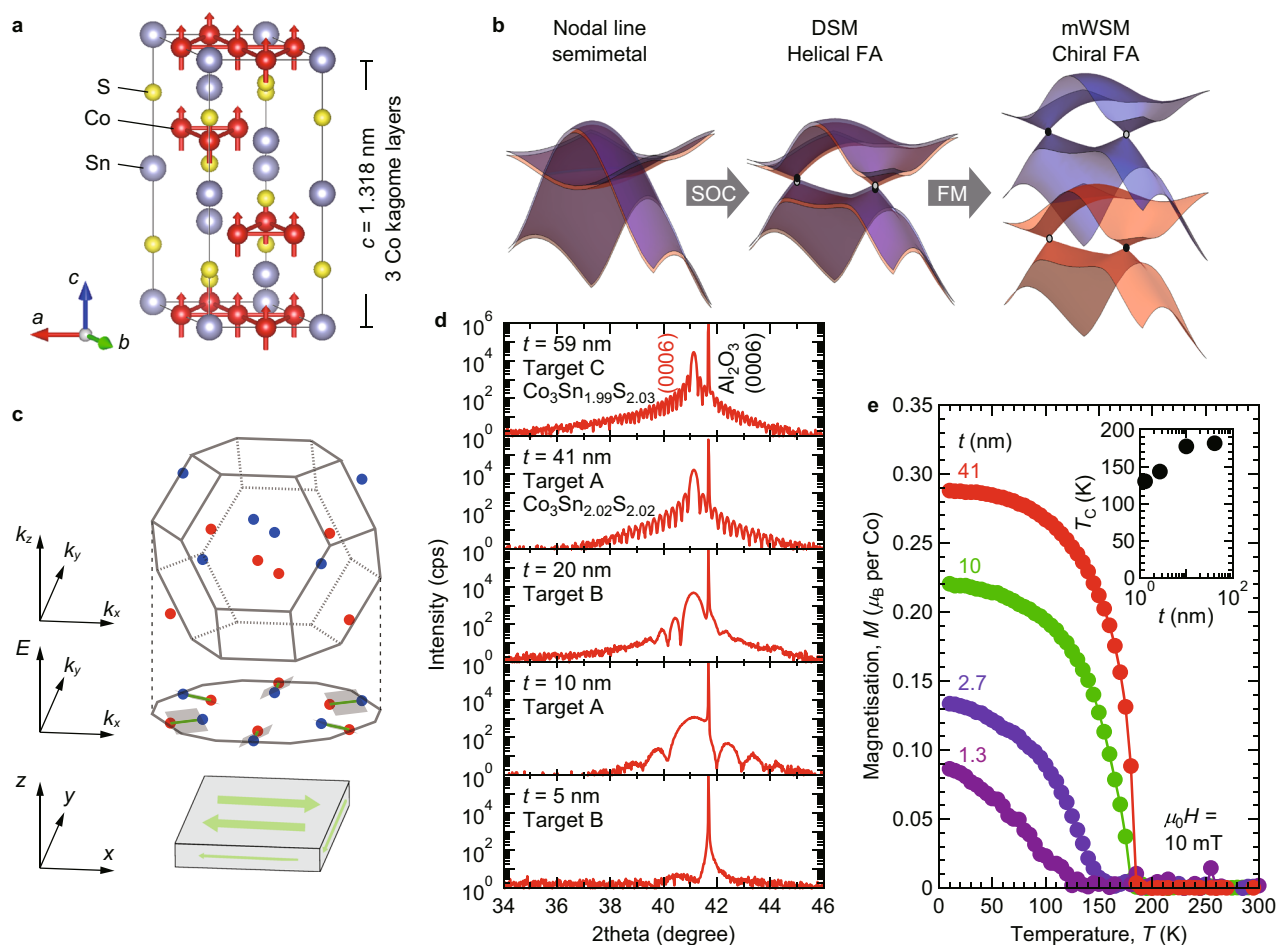


**Fig. 1** Thin films of kagome-lattice ferromagnet  $\text{Co}_3\text{Sn}_2\text{S}_2$ . **a** Crystal structure of  $\text{Co}_3\text{Sn}_2\text{S}_2$  and the ferromagnetic spin ordering below  $T_C$  drawn with VESTA<sup>28</sup>. **b** Schematic band structures of nodal line semimetal, DSM, mWSM (FM: ferromagnetic coupling). Band crossing points, that is, Dirac and Weyl points, are represented by black and grey ellipsoids. **c** Distribution of Weyl points in energy-wave number ( $E$ - $k$ ) space and electrical conduction via chiral FA states in real space. Weyl points with opposite spin chiralities are represented by red and blue circles. **d** Typical out-of-plane XRD patterns of  $\text{Co}_3\text{Sn}_2\text{S}_2$  films with varied  $t$ . Three different targets (A, B and C) were used to check the reproducibility of the film composition and quality. For  $t \geq 40$  nm, the film compositions determined by EDX are shown. **e**  $M$  versus  $T$  curves measured for  $t = 41, 10, 2.7$  and  $1.3$  nm (fabricated with the target A) at  $\mu_0 H = 10$  mT. The inset shows the  $t$  dependence of  $T_C$ .

island-like polycrystalline domains, the mWSM phase with large anomalous Hall effect (AHE) emerges above a critical thickness of  $\sim 10$  nm.

## Results

**Film growth and magnetisation measurements.** We fabricated  $c$  axis oriented  $\text{Co}_3\text{Sn}_2\text{S}_2$  films on  $\text{Al}_2\text{O}_3(0001)$  substrates by co-sputtering technique<sup>22</sup> (Method). The  $t$  was controlled from nominal 1.3 nm (roughly one unit cell) to 61 nm. Figure 1d shows typical X-ray diffraction (XRD) patterns of nearly stoichiometric  $\text{Co}_3\text{Sn}_2\text{S}_2$  films capped with  $\text{SiO}_x$  (a thickness of  $\sim 50$  nm), where the systematic variation of thickness fringes indicates the uniform film quality and tunable manner of our  $t$  control at least down to  $t \sim 10$  nm (Supplementary Figs. 1 and 2). Although the diffraction intensity for  $t < 4$  nm was very weak, the deposition rate for these films was reliably reproducible by the sputtering method. The surface morphology of thin films for  $t = 4$  and 11 nm was fairly flat (Supplementary Fig. 3). Based on these observations, we apply the nominal value of  $t$  estimated from the deposition rate in the following discussions.

Figure 1e shows magnetisation  $M$  versus temperature  $T$  curves measured for films with nominal  $t$  values of 41, 10, 2.7 and 1.3 nm. A sharp rise in  $M$  occurs, respectively, at  $T = 181$ , 177, 143 and 130 K, which correspond to Curie temperature  $T_C$ . For  $t = 41$  nm, the saturated value of  $M$  ( $M_s$ ) of  $0.29 \mu_B$  per Co (where  $\mu_B$  is Bohr magneton) at  $T = 10$  K is comparable to the reported bulk value of  $0.29\text{--}0.33 \mu_B$  per Co<sup>5–7,16,17</sup>. With decreasing  $t$ , both the  $M_s$  and the  $T_C$  (inset) decrease monotonically. Considering the Stoner mechanism<sup>16,17</sup>, these decreases are induced by the reduction of the density of states (DOS) at  $E_F$  in the ultrathin films. In fact, the Hall coefficient  $R_H$  in the paramagnetic state is systematically decreased<sup>23</sup> (see Supplementary Fig. 4). Given that  $\text{Co}_3\text{Sn}_2\text{S}_2$  thin films have semimetallic bands as in the bulk, the decrease in  $R_H$  should correspond to the decrease of carriers that contribute to the ordinary Hall effect, that is, the decrease in the DOS at  $E_F$ . However, the monotonous systematic trend of  $M$ ,  $T_C$  and  $R_H$  at  $t > 4$  nm in Supplementary Fig. 4 allows us to extrapolate the finite value of  $R_H$  in the ultrathin region, indicating that the ferromagnetic order is maintained with finite DOS even in the ultrathin films.

**Structure-property relationship in  $\text{Co}_3\text{Sn}_2\text{S}_2$  films.** In contrast to these monotonous changes in magnetism, electrical resistivity  $\rho_{xx}$  ( $=R_s \times t$ , where  $R_s$  is the measured sheet resistance) dramatically increases with the  $t$  reduction. In Fig. 2a, b, the  $t$  dependences of  $\rho_{xx}$  at (a)  $T = 200 \text{ K} > T_C$  and (b)  $2 \text{ K} < T_C$  are shown, respectively. Here,  $\rho_{xx}$  is estimated based on the assumption that electrical conduction is uniform over the whole region of a film without surface conduction. Above approximately  $t = 15$  nm, both  $\rho_{xx}$  values at  $T = 200 \text{ K}$  and  $2 \text{ K}$  are virtually constant; the bulk component of electrical conduction is comparable in these thick films. In the intermediate range of  $\sim 3 \text{ nm} < t < \sim 15 \text{ nm}$ ,  $\rho_{xx}$  at  $T = 200 \text{ K}$  increases as  $t$  decreases, whereas  $\rho_{xx}$  at  $T = 2 \text{ K}$  increases more significantly with a rough relation of  $\rho_{xx} \propto t^{-1}$ . Below  $t \sim 3 \text{ nm}$ , the electrical resistance exceeds the measurement limit. To comprehensively understand the impact of  $t$  on  $\rho_{xx}$  and also magnetism, we performed cross-sectional transmission electron microscopy (TEM) experiments for typical samples in these three  $t$  regions (nominal  $t = 45$ , 10 and 2.7 nm), as displayed in Fig. 2c–e. The 45-nm-thick sample is flat and the nominal  $t$  value estimated from the deposition rate is in excellent agreement with the  $t$  ( $t_{\text{obs}}$ ) value observed by TEM. In the 10-nm-thick sample, crystalline domains form a continuous network albeit with  $t_{\text{obs}}$  fluctuating between 8 and 12 nm. Island-like

polycrystalline domains eventually appear in the nominal 2.7-nm-thick sample ( $t_{\text{obs}} = 0\text{--}6 \text{ nm}$ ). Overall, the averaged  $t_{\text{obs}}$  matches well with the nominal  $t$  value, guaranteeing that our calculation of  $M$  using the film volume is reasonable (Fig. 1e). Figure 2f–h show the magnetic field  $\mu_0 H$  dependences of  $M$ , where  $\mu_0$  is the vacuum permeability and  $H$  is magnetic field strength (also see Supplementary Fig. 5 for Hall resistivity  $\rho_{yx}$  data). A clear hysteresis of  $M$  is observed for nominal  $t$  values of 41, 10 and 2.7 nm at  $T = 100 \text{ K}$ . Please note that the coercive field is too large to measure hysteresis loops for  $t > 10 \text{ nm}$  at  $T < 100 \text{ K}$  in our apparatus with an upper limit of  $7 \text{ T}$ <sup>22</sup>. The ferromagnetic hysteresis with comparably large  $M$  is also obtained for nominal  $t = 2.7 \text{ nm}$  while the coercive field becomes small with decreasing  $t$ . As shown in Supplementary Fig. 5d–f,  $\rho_{yx}$  of all films with  $t = 41$ , 10 and 4 nm show hysteresis behaviour at  $T = 100 \text{ K}$ . Judging from the consistent hysteresis character of  $M$  and  $\rho_{yx}$  in Fig. 2f–h and Supplementary Fig. 5d–f, we confirmed the AHE origin of the observed  $\rho_{yx}$  as being consistent to the bulk<sup>5,6</sup> based on the intrinsic mechanism<sup>24</sup>. The systematic comparison of these data shows that the high resistance exceeding the measurement limit in the ultrathin films with nominal  $t < \sim 3 \text{ nm}$  arises from the formation of island-like polycrystalline domains, while the ferromagnetism persists with perpendicular magnetic anisotropy (Fig. 2h). More importantly, the samples with  $t = 45$  and 10 nm exhibit the distinct  $\rho_{xx}$  behaviour (Fig. 2a, b) despite insignificant differences in their film qualities (Figs. 1d, 2c, d, and Supplementary Figs. 1 and 2), which signals a qualitative change in the conduction mechanism between these samples.

**Thickness dependence of electrical and AHE properties.** The anomalous electrical transport properties are pronounced on the  $t$  dependent systematic variation in Fig. 3. As shown in Fig. 3a, thick films with  $t \geq 20 \text{ nm}$  exhibit metallic behaviour down to the lowest  $T$  of 2 K. The  $\rho_{xx}$  shows an inflection near  $T = 180 \text{ K}$ , which agrees well with  $T_C$  detected by magnetisation measurements (Fig. 1e). In addition, two samples for  $t = 41$  and 59 nm (broken lines) represent superior conductive behaviour in low  $T$  region with a comparable residual resistivity ratio to that for bulk single crystals<sup>5–7,10</sup>. A decrease in  $t$  to  $< 10 \text{ nm}$  substantially increases the  $\rho_{xx}$  without an inflection around  $T_C$  ( $t = 5$  and 4 nm) although  $M$  develops ferromagnetically. The  $\rho_{xx}$  for the films with nominal  $t = 2.7$  and 1.3 nm was undetectable above the measurement limit (Fig. 2a, b) because of the disconnection of film domains (Fig. 2e). In Hall conductivity,  $\sigma_{xy} = \frac{\rho_{yx}}{\rho_{xx} + \rho_{yy}^2}$  (Supplementary Fig. 6a for the  $T$  dependence of  $\rho_{yx}$ ) in Fig. 3b, the  $\sigma_{xy}$  dramatically increases at  $T$  comparable with  $T_C$  for  $M$  (Fig. 1e) and saturates at low  $T$ . Although many of the thick films ( $t > 10 \text{ nm}$ ) show  $\sigma_{xy}$  exceeding  $1000 \Omega^{-1} \text{ cm}^{-1}$  at  $T = 2 \text{ K}$ , which is comparable or even higher than the bulk values<sup>5,6</sup> and theoretically calculated values<sup>5,12</sup>, the  $\sigma_{xy}$  for  $t = 5$  and 4 nm is much suppressed. These bulk-comparable  $T$ -dependent  $\rho_{xx}$  and  $\sigma_{xy}$  strongly support that the AHE character in thick films  $t > 10 \text{ nm}$  reflects the Weyl features of electronic bands. In addition to the high  $\sigma_{xy}$ , we observed a negative magnetoresistance in an in-plane  $H$  configuration, called the chiral anomaly<sup>2–4,25</sup>, which has been discussed as a hallmark of the mWSM state<sup>5</sup> (Supplementary Fig. 7).

To find the surface-specific conductance contributions by surface FAs (Fig. 1c), we plot sheet conductance  $\frac{1}{R_s} = \frac{t}{\rho_{xx}^{\text{bulk}}} + \sigma_s$  as a function of  $t$  in Fig. 3c, where  $\rho_{xx}^{\text{bulk}}$  is the bulk resistivity of  $\text{Co}_3\text{Sn}_2\text{S}_2$  film and  $\sigma_s$  is the  $t$ -independent surface conductance. We here summarise all data acquired for films fabricated with the three sputtering targets A (circles), B (triangles) and C (squares)

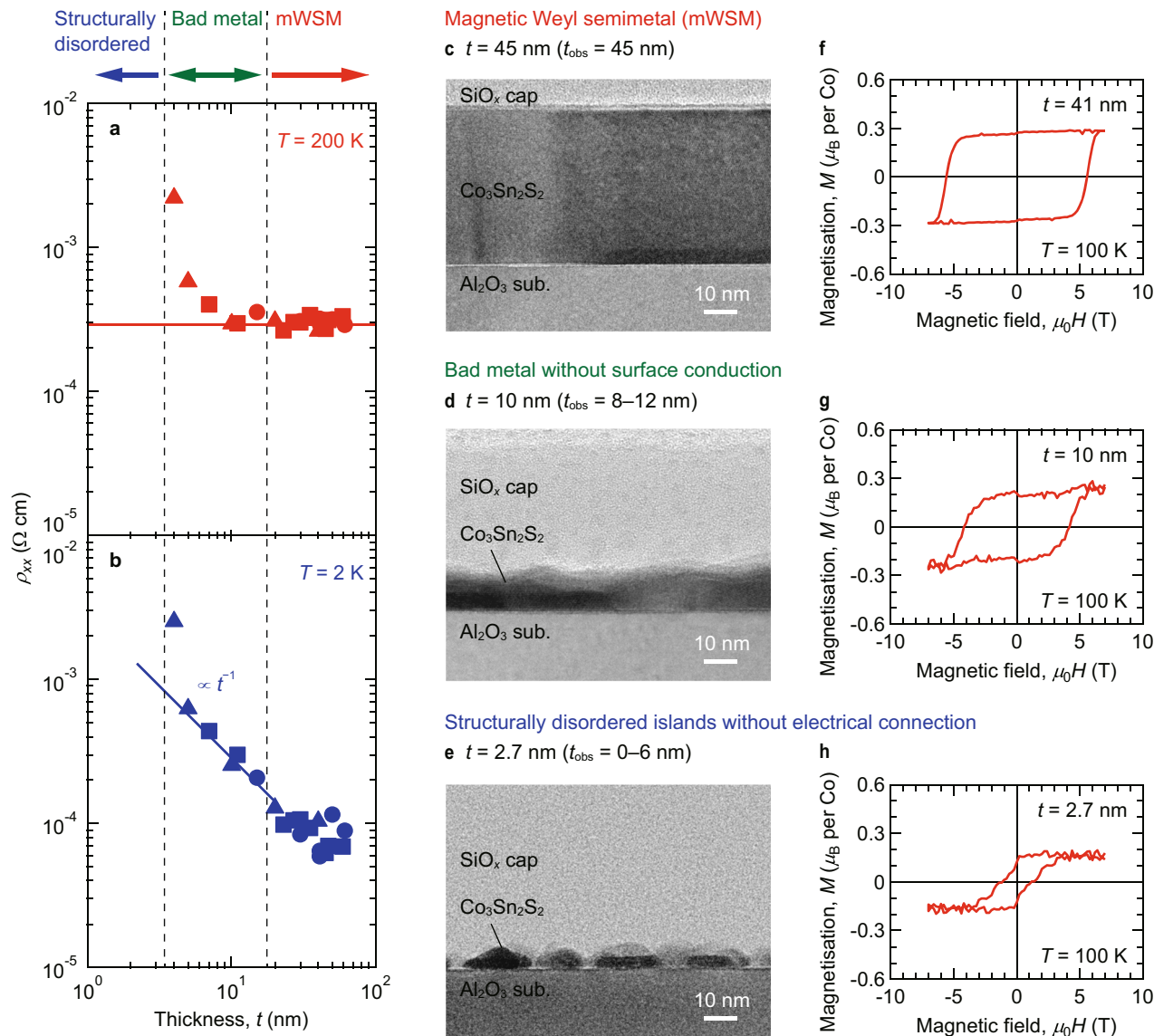


**Fig. 2 Structure-property relationship.** **a, b**  $t$  dependence of  $\rho_{xx}$  at  $T = 200$  K and  $2$  K, respectively. The symbols in **a** and **b** correspond to the used sputtering targets: A (circles), B (triangles) and C (squares). The red solid line in **a** is a guide to the eye, corresponding to the value of  $\rho_{xx}^{\text{bulk}} = 2.9 \times 10^{-4} \Omega \text{ cm}$ . The blue solid line in **b** represents a rough relation of  $\rho_{xx} \propto t^{-1}$ . These data suggest three  $t$  regions with distinct conduction mechanisms: mWSM for  $t > 15$  nm, bad metal without surface conduction for  $-3 \text{ nm} < t < 15$  nm, and structurally disordered islands without electrical connection for  $t < -3$  nm. **c–e** Cross-sectional TEM images for  $t = 45$ ,  $10$  and  $2.7$  (nominal) nm, respectively. The  $t_{\text{obs}}$  values represent rough thicknesses of  $\text{Co}_3\text{Sn}_2\text{S}_2$  estimated from the TEM images. **f–h**  $M$  versus  $\mu_0 H$  curves for  $t = 41$ ,  $10$  and  $2.7$  (nominal) nm, respectively. The used sputtering targets were A for **e–h**, B for **d**, and C for **c**.

to see the overall tendency and reproducibility. In the paramagnetic state at  $T = 200$  K, a reliable linear fit to the data yields  $\rho_{xx}^{\text{bulk}} = 2.9 \times 10^{-4} \Omega \text{ cm}$  (Fig. 2a) and a  $t$  offset of  $1.1$  nm. This linear relation indicates that the electrical conduction in the paramagnetic state for  $t = 5\text{--}61$  nm is well dominated and reproduced by  $\rho_{xx}^{\text{bulk}}$ . In contrast, a finite  $R_s^{-1}$  offset, which corresponds to the surface conductance  $\sigma_s$ , is extracted from the data for  $t > 20$  nm at  $T = 2$  K (indicated by the black arrow). There seem two sample groups with different  $\sigma_s$  (the blue solid and dashed lines); the detailed analysis will be reported elsewhere. The  $\sigma_{xy}$  in Fig. 3d initiates to increase above  $10$  nm with saturation in the thicker region. The  $\sigma_{xy}$  in the mWSM is discussed to be proportional to the distance between two Weyl points with opposite chiralities in  $k$ -space<sup>1,26</sup>. Under the overall ferromagnetic condition against  $t$  variation, the gradual increase of  $\sigma_{xy}$  with increasing  $t$  reflects the development of pairs of Weyl nodes in the electronic bands, resulting in the simultaneous

emergence of conductance contribution by the projected surface FAs at  $t > 20$  nm. These significant variations reveal the presence of a critical thickness of  $\text{Co}_3\text{Sn}_2\text{S}_2$  films hindering a feature of mWSM.

**Stability of mWSM phase in  $\text{Co}_3\text{Sn}_2\text{S}_2$  films.** Using  $\sigma_{xy}$  and electrical conductivity  $\sigma_{xx} = \frac{\rho_{xx}}{\rho_{xx} + \rho_{yx}}$ , we calculated a tangent of the Hall angle for AHE,  $\sigma_{xy}/\sigma_{xx}$ , which is directly linked to the Berry curvature of electronic bands in the intrinsic mechanism<sup>24</sup>. As shown in Fig. 4a, the  $40$ -nm-thick film exhibits  $\sigma_{xy}/\sigma_{xx}$  as large as  $0.24$  at  $T = 130$  K. With a decrease in  $t$ , the  $T$  at which  $\sigma_{xy}/\sigma_{xx}$  becomes the largest shifts to low  $T$ . The  $T$ -dependent  $\sigma_{xy}/\sigma_{xx}$  can be apparently classified to two trends with/without peak at finite  $T$  (Supplementary Fig. 6b), which indicates that the AHE in all films is governed by the intrinsic mechanism identical to that for the bulk with different  $T$ -dependent  $\sigma_{xx}$

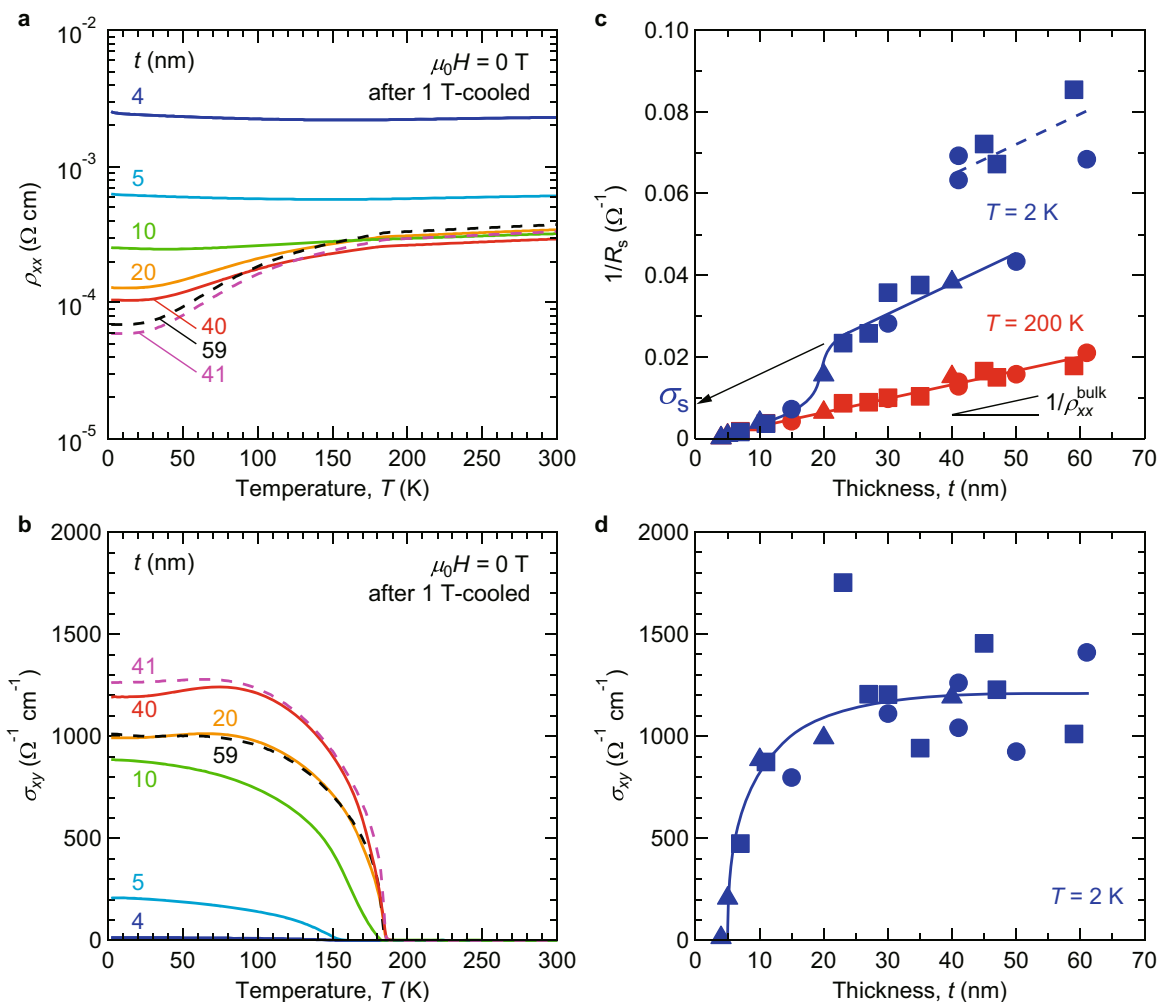


**Fig. 3 Critical  $t$  for the emergence of Weyl features in electrical transport properties.** **a**,  $T$  dependence of  $\rho_{xx}$  and  $\sigma_{xy}$  measured at zero field after field-cooled at  $\mu_0 H = 1$  T, respectively. The used sputtering targets were A for  $t = 41$  nm, B for  $t = 40, 20, 10, 5$  and  $4$  nm, and C for  $t = 59$  nm. **c**  $t$  dependence of  $R_s^{-1}$  at  $T = 2$  K (blue symbols) and  $200$  K (red symbols). The red solid line is a linear fit to the data at  $T = 200$  K. The blue solid and dashed lines for the data at  $T = 2$  K represent two sample groups with different  $\sigma_s$  values. The blue solid curve is a guide to the eye. **d**  $t$  dependence of  $\sigma_{xy}$  at  $T = 2$  K. The blue solid curve is a guide to the eye. Symbols in **c** and **d** correspond to the used sputtering targets: A (circles), B (triangles) and C (squares).

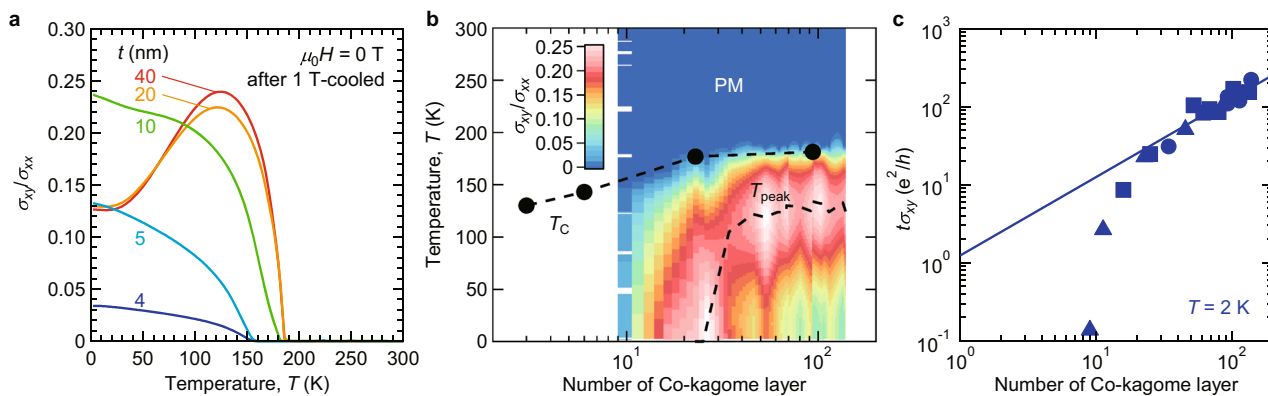


**Fig. 4 Phase diagram of  $\text{Co}_3\text{Sn}_2\text{S}_2$  films for magnetic WSM.** **a**  $T$  dependence of  $\sigma_{xy}/\sigma_{xx}$  measured for films with  $t = 40, 20, 10, 5$  and  $4$  nm (fabricated with the target B) at zero field after field-cooled at  $\mu_0 H = 1$  T. **b** Contour plot of  $\sigma_{xy}/\sigma_{xx}$  as a function of  $T$  and the nominal number of Co-kagome layers in the  $\text{Co}_3\text{Sn}_2\text{S}_2$  films (PM: paramagnetic). The nominal number of Co-kagome layers was calculated using the  $c$  axis length determined by XRD (Supplementary Fig. 1).  $T_C$  (Fig. 1e) and  $T_{\text{peak}}$  are included for comparison. **c** Sheet Hall conductivity  $t\sigma_{xy}$  at  $T = 2$  K as a function of the number of Co-kagome layers. The solid line indicates the fitting result using a linear relation of  $\log t\sigma_{xy} = a + \log N_{\text{Co}}$ .

(Supplementary Fig. 8). To emphasise this trend, we made a contour plot of the  $\sigma_{xy}/\sigma_{xx}$  as functions of  $T$  and the sample thickness in Fig. 4b, where the nominal number of Co-kagome layers (three Co-kagome layers  $\sim 1.3$  nm) is used as the sample thickness instead of  $t$ . The  $T_C$  values (black circles) determined by magnetisation measurements (Fig. 1e) define the ferromagnetic/paramagnetic regions in the diagram. As discussed in Figs. 1e and 2, the average one- and two-unit-cells-thick samples with island-like polycrystalline domains maintain the ferromagnetic ordering, securing that the time reversal symmetry is broken in overall  $t$  regions. It is now more obvious that a large- $\sigma_{xy}/\sigma_{xx}$  region vanishes below a few tens Co-kagome layers, unveiling a mWSM phase emerges in the thicker region. The linear dispersive electronic bands would be intrinsically diminished in the thinner  $t$  region similarly to band renormalisation in DSM of  $\text{Cd}_3\text{As}_2$  thin film<sup>15,27</sup>. Though it is difficult to fully understand the additional role of disorder by lattice distortion and roughness in the disappearance of AHE in the ultrathin films, the intrinsic band modification in ultrathin films may be examined in future study by spectroscopy after overcoming the difficulty of surface treatment or exfoliation.

## Discussion

The final remark in this study is the verification of quantum Hall conductance  $e^2/h$  ( $e$ : elementary charge,  $h$ : Planck constant) of one Co-kagome layer in the mWSM by a systematic extrapolation of sheet Hall conductance  $t\sigma_{xy}$  shown in Fig. 4c, which has been theoretically expected in kagome layer with a flat band feature<sup>5,11,12</sup>. The good agreement of a linear relationship in the certain region may exemplify the two-dimensional contribution of each Co-kagome layer to the Hall conductivity with close  $E_F$  to the gap. In comparison with the  $1.28 e^2/h$  in each kagome layer calculated from the  $\sigma_{xy}$  value of  $1130 \Omega^{-1} \text{cm}^{-1}$  for bulk crystal<sup>5</sup>, the extrapolated value of  $1.3 e^2/h$  by fitting in Fig. 4c using a linear relation of  $\log t\sigma_{xy} = a + \log N_{\text{Co}}$ , where  $a$  is a fitting parameter and  $N_{\text{Co}}$  is the number of Co-kagome layer, is further reasonable (Supplementary Fig. 9). The robust ferromagnetism in the ultrathin films, large AHE, and a verification of quantum conductance experimentally prove the significant feature of mWSM  $\text{Co}_3\text{Sn}_2\text{S}_2$  thin films. Stabilisation of ultimate thin-limit of Co-kagome monolayer is a future interesting challenge to perform direct measurement of magnetic interaction in the layer and quantum conductance. In view of a wide variety of mWSMs and magnets with kagome lattice, heterostructure engineering and  $E_F$  tuning will pave a way to find emergent phenomena that relate with Weyl nodes.

## Methods

**Thin-film growth.** The  $\text{Co}_3\text{Sn}_2\text{S}_2$  films were grown on  $\text{Al}_2\text{O}_3(0001)$  substrates by radio-frequency magnetron sputtering<sup>22</sup> with Co– $\text{SnS}_{1.35}$  mosaic targets. The mosaic target was prepared using an  $\text{SnS}_{1.35}$  disc (mixed-phase of  $\text{SnS}$  and  $\text{SnS}_2$ ) and Co metal chips. The film composition was controlled by the number and location of the Co metal chips. Three Co– $\text{SnS}_{1.35}$  mosaic targets were used, which are referred to as A, B and C in the text. To suppress possible influences by impurities, e.g., unreacted/segregated ferromagnetic Co, particular attention was paid to the reproducibility of the film composition using the three different targets. Prior to the film growth, the substrates were annealed at  $1000^\circ\text{C}$  in air to obtain atomically smooth surfaces. The films were deposited at  $400^\circ\text{C}$  and then capped with  $\text{SiO}_x$ , followed by in situ annealing at  $800^\circ\text{C}$  in a vacuum. The crystal structure and composition of the films were analysed by XRD using  $\text{Cu } K_\alpha$  radiation and energy-dispersive X-ray spectroscopy, respectively.

**Electrical and magnetic measurements.** Electrical measurements were performed with a Physical Property Measurement System (Quantum Design, Inc.). A Hall-bar shaped channel was patterned by mechanically scratching the film. Electrical contacts were made with indium solder. The measured  $\rho_{yx}$  versus  $\mu_0H$  curves were anti-symmetrized. The  $T$  dependence of  $\rho_{yx}$  was obtained by anti-symmetrizing data taken at zero field after field-cooled at  $\mu_0H = \pm 1$  T. Magnetisation measurements were performed with a Magnetic Property Measurement System (Quantum

Design, Inc.). Before the measurements, the bottom surface of  $\text{Al}_2\text{O}_3$  substrate was polished to remove possible magnetic contaminations from the substrate holder used. For the  $M$  versus  $T$  measurements in Fig. 1e, the samples were cooled from  $T = 300$  K to 10 K in an out-of-plane magnetic field of  $\mu_0H = 1$  T. Subsequently,  $M$  at  $\mu_0H = 10$  mT was measured in a heating process. The measured  $M$  versus  $\mu_0H$  curves were anti-symmetrized for a comparison with  $\rho_{yx}$  versus  $\mu_0H$  characteristics.

## Data availability

The data that support the findings of this study are available from the corresponding author upon reasonable request.

Received: 1 September 2020; Accepted: 22 January 2021;

Published online: 18 February 2021

## References

- Vafeek, O. & Vishwanath, A. Dirac fermions in solids: from high- $T_C$  cuprates and graphene to topological insulators and Weyl semimetals. *Annu. Rev. Condens. Matter Phys.* **5**, 83–112 (2014).
- Yan, B. & Felsner, C. Topological materials: Weyl semimetals. *Annu. Rev. Condens. Matter Phys.* **8**, 337–354 (2017).
- Armitage, N. P., Mele, E. J. & Vishwanath, A. Weyl and Dirac semimetals in three-dimensional solids. *Rev. Mod. Phys.* **90**, 015001 (2018).
- Nagaosa, N., Morimoto, T. & Tokura, Y. Transport, magnetic and optical properties of Weyl materials. *Nat. Rev. Mater.* **5**, 621–636 (2020).
- Liu, E. et al. Giant anomalous Hall effect in a ferromagnetic kagome-lattice semimetal. *Nat. Phys.* **14**, 1125–1131 (2018).
- Wang, Q. et al. Large intrinsic anomalous Hall effect in half-metallic ferromagnet  $\text{Co}_3\text{Sn}_2\text{S}_2$  with magnetic Weyl fermions. *Nat. Commun.* **9**, 3681 (2018).
- Guin, S. N. et al. Zero-field Nernst effect in a ferromagnetic kagome-lattice Weyl-semimetal  $\text{Co}_3\text{Sn}_2\text{S}_2$ . *Adv. Mater.* **31**, 1806622 (2019).
- Li, G. et al. Surface states in bulk single crystal of topological semimetal  $\text{Co}_3\text{Sn}_2\text{S}_2$  toward water oxidation. *Sci. Adv.* **5**, eaaw9867 (2019).
- Morali, N. et al. Fermi-arc diversity on surface terminations of the magnetic Weyl semimetal  $\text{Co}_3\text{Sn}_2\text{S}_2$ . *Science* **365**, 1286–1291 (2019).
- Liu, D. F. et al. Magnetic Weyl semimetal phase in a kagome crystal. *Science* **365**, 1282–1285 (2019).
- Ohgushi, K., Murakami, S. & Nagaosa, N. Spin anisotropy and quantum Hall effect in the kagome lattice: chiral spin state based on a ferromagnet. *Phys. Rev. B* **62**, R6065–R6068 (2000).
- Muechler, L. et al. Emerging chiral edge states from the confinement of a magnetic Weyl semimetal in  $\text{Co}_3\text{Sn}_2\text{S}_2$ . *Phys. Rev. B* **101**, 115106 (2020).
- Qi, X.-L. & Zhang, S.-C. Topological insulators and superconductors. *Rev. Mod. Phys.* **83**, 1057–1110 (2011).
- Chang, C.-Z. & Li, M. Quantum anomalous Hall effect in time-reversal-symmetry breaking topological insulators. *J. Phys.: Condens. Matter* **28**, 123002 (2016).
- Wang, Z., Weng, H., Wu, Q., Dai, X. & Fang, Z. Three-dimensional Dirac semimetal and quantum transport in  $\text{Cd}_3\text{As}_2$ . *Phys. Rev. B* **88**, 125427 (2013).
- Schnelle, W. et al. Ferromagnetic ordering and half-metallic state of  $\text{Sn}_2\text{Co}_3\text{S}_2$  with the shandite-type structure. *Phys. Rev. B* **88**, 144404 (2013).
- Ozawa, A. & Nomura, K. Two-orbital effective model for magnetic Weyl semimetal in kagome-lattice shandite. *J. Phys. Soc. Jpn.* **88**, 123703 (2019).
- Huang, B. et al. Layer-dependent ferromagnetism in a van der Waals crystal down to the monolayer limit. *Nature* **546**, 270–273 (2017).
- Gong, C. et al. Discovery of intrinsic ferromagnetism in two-dimensional van der Waals crystals. *Nature* **546**, 265–269 (2017).
- Heinrich, B. & Cochran, J. F. Ultrathin metallic magnetic films: magnetic anisotropies and exchange interactions. *Adv. Phys.* **42**, 523–639 (1993).
- Schneider, C. M. et al. Curie temperature of ultrathin films of fcc-cobalt epitaxially grown on atomically flat  $\text{Cu}(100)$  surfaces. *Phys. Rev. Lett.* **64**, 1059 (1990).
- Fujiwara, K. et al. Ferromagnetic  $\text{Co}_3\text{Sn}_2\text{S}_2$  thin films fabricated by co-sputtering. *Jpn. J. Appl. Phys.* **58**, 050912 (2019).
- Yang, R. et al. Magnetization-induced band shift in ferromagnetic Weyl semimetal  $\text{Co}_3\text{Sn}_2\text{S}_2$ . *Phys. Rev. Lett.* **124**, 077403 (2020).
- Nagaosa, N., Sinova, J., Onoda, S., MacDonald, A. H. & Ong, N. P. Anomalous Hall effect. *Rev. Mod. Phys.* **82**, 1539–1592 (2010).

25. Nielsen, H. B. & Ninomiya, M. The Adler-Bell-Jackiw anomaly and Weyl fermions in a crystal. *Phys. Lett. B* **130**, 389–396 (1983).
26. Burkov, A. Anomalous Hall effect in Weyl metals. *Phys. Rev. Lett.* **113**, 187202 (2014).
27. Uchida, M. et al. Quantum Hall states observed in thin films of Dirac semimetal Cd<sub>3</sub>As<sub>2</sub>. *Nat. Commun.* **8**, 2274 (2017).
28. Momma, K. & Izumi, F. VESTA 3 for three-dimensional visualization of crystal, volumetric and morphology data. *J. Appl. Cryst.* **44**, 1272–1276 (2011).

### Acknowledgements

The authors are grateful to K. Kobayashi, Y. Yanagi, M.-T. Suzuki and Y. Motome for fruitful discussions. This work was performed under the Inter-University Cooperative Research Program of the Institute for Materials Research, Tohoku University (proposal no. 19G0410). This work was supported by JSPS KAKENHI (Grant No. 20H01830) and JST CREST (JPMJCR18T2).

### Author contributions

J.I. and K.F. grew the films and measured the electrical transport properties. J.S. performed the magnetoresistance measurements. K.F. performed the magnetisation measurements under the support by J.S., T.S. and K.T. J.I. and K.F. analysed the measured data. K.N. contributed to theoretical interpretations of the experimental results. J.I., K.F. and A.T. wrote the manuscript with input from other authors. All authors discussed the results. A.T. supervised the project.

### Competing interests

The authors declare no competing interests.

### Additional information

**Supplementary information** The online version contains supplementary material available at <https://doi.org/10.1038/s43246-021-00122-5>.

**Correspondence** and requests for materials should be addressed to K.F. or A.T.

**Peer review information** Primary handling editor: Aldo Isidori.

**Reprints and permission information** is available at <http://www.nature.com/reprints>

**Publisher's note** Springer Nature remains neutral with regard to jurisdictional claims in published maps and institutional affiliations.



**Open Access** This article is licensed under a Creative Commons Attribution 4.0 International License, which permits use, sharing, adaptation, distribution and reproduction in any medium or format, as long as you give appropriate credit to the original author(s) and the source, provide a link to the Creative Commons license, and indicate if changes were made. The images or other third party material in this article are included in the article's Creative Commons license, unless indicated otherwise in a credit line to the material. If material is not included in the article's Creative Commons license and your intended use is not permitted by statutory regulation or exceeds the permitted use, you will need to obtain permission directly from the copyright holder. To view a copy of this license, visit <http://creativecommons.org/licenses/by/4.0/>.

© The Author(s) 2021